Solid–Liquid Phase Behavior of Ternary Mixtures

Brian C. Attwood and Carol K. Hall
Dept. of Chemical Engineering, North Carolina State University, Raleigh, NC 27695

DOI 10.1002/aic.11513
Published online May 22, 2008 in Wiley InterScience (www.interscience.wiley.com).

The Gibbs Duhem integration technique is extended to calculate ternary phase diagrams at constant temperature and pressure. The technique is used to calculate solid–liquid–vapor phase equilibria for a system selected to roughly model a mixture of two diastereomeric molecules of similar melting point and diameter immersed in a solvent with a lower melting point and a slightly smaller diameter. The cross-species well-depth and diameter between the two diastereomers are varied to determine their impact on the phase equilibria. We find that when the interspecies well-depth is lowered to less than that of either of the diastereomers, the solid phase separates into two solid solutions and consequently there is a region of three-phase coexistence in the ternary phase diagram. We then calculate ternary phase diagrams at a series of temperatures for one set of molecular parameters. For an equimolar mixture of diastereomers, there is a range of temperature and solvent concentration at which only one of the diastereomers will precipitate, thus effecting a separation of the diastereomers. As the temperature is decreased the purity of the precipitate increases. © 2008 American Institute of Chemical Engineers *AIChE J,* 54: 1886–1894, 2008
Keywords: solid-liquid equilibria, ternary phase diagrams classical resolution

Introduction

Knowledge of the equilibria between solids and fluids is of vital importance in designing industrial processes based on crystallization, including separations, purification, concentration, solidification, and analysis. Crystallization is widely used in the pharmaceutical industry for product recovery because it yields high-purity products with a relatively low energy expenditure compared to distillation or other common methods of separation. For chiral drugs, crystallization is one of several means of separation.[1] Chiral drugs are normally produced as a mixture of two racemates. In general, one of the racemates is the active ingredient; the other is either inactive or has some unwanted activity. Although it desirable to separate the racemates, this cannot be done through standard techniques because the racemates have identical thermophysical properties. This problem can be circumvented through the use of diastereomeric crystallization techniques, which are also known as classical resolution.[2] The two racemates are first reacted with a chiral resolving agent, forming a pair of diastereomers that are chemically identical but have different physical properties. The diastereomers are then separated using fractional crystallization, taking advantage of the now-differing solubilities of the two components. Despite the considerable industrial interest in classical resolution of chiral products, relatively little research is available in the literature on the phase equilibria of chiral products or the optimization of the processes used to separate them.[3–5] Crystallization has economic benefits over distillation for components with melting points near ambient conditions because of lower energy requirements. The lower operating temperatures typically used in crystallization processes are also important when separating components that would decompose at the temperatures necessary for distillation.[6] Crystallization is also used in the desalination and decontamination of wastewater streams.[7]

Correspondence concerning this article should be addressed to C. K. Hall at hall@turbo.che.ncsu.edu.

A prerequisite to efficient use of crystallization is knowledge of the solid–liquid phase equilibria of the components to be separated. The solid–liquid phase diagram for a mixture has many uses in the design of a fractional crystallization process. It can be used to identify feasible operation paths given a known feed stream, to choose optimal operating conditions, and to solve the related mass balances in a separation operation.[8] Although the solid–liquid phase diagram for a particular substance or mixture can be obtained by experiment, limitations on time and resources generally allow for only a small sampling of possible operating conditions for any given system. Theory and molecular-level simulation can overcome some of these limitations by making it possible to gain insight into the phase equilibria of whole classes of mixtures, rather than just one in particular. In this work, we use simulation to gain a fundamental understanding of how molecular size and attractions affect the solid–fluid phase equilibria of ternary mixtures of Lennard-Jones molecules.

In this article, we seek to gain a fundamental understanding of what role molecular parameters, such as the Lennard-Jones well-depth and diameter, play in crystallization of ternary mixtures. The system investigated is that of a model diastereomeric mixture, composed of Lennard-Jones particles. The two diastereomer molecules have similar Lennard-Jones well-depths and diameters and, hence, melting points, while the solvent has a much lower melting point to prevent it from crystallizing with the diastereomers. Ternary phase diagrams for the system are calculated at constant temperature and pressure using the Gibbs Duhem integration technique. The Gibbs Duhem integration technique is well-suited for calculating solid–liquid phase equilibria because it does not require the insertion of molecules into dense liquid and solid phases as do other popular simulation techniques such as the Gibbs ensemble. It was originally proposed by Kofke and used to calculate the vapor–liquid phase equilibria of pure Lennard-Jones fluids.[9,10] Later, the technique was extended to multiphase equilibria and used to calculate solid–fluid phase equilibria in binary mixtures.[11,12] To our knowledge, this is the first time the Gibbs Duhem technique has been applied to phase equilibria for ternary mixtures. By varying the cross-species well-depths and molecular diameters associated with the two diastereomers we learn how these parameters affect the resulting ternary phase behavior. The effect of temperature is then explored by calculating phase diagrams over a range of temperatures for a given set of cross-species well-depths and molecular diameters.

Highlights of the results are the following. The ternary Gibbs Duhem integration technique that we developed is well-behaved in that when there is no liquid–liquid or solid–solid immiscibility, the coexistence curves connect one initial coexistence point to the other in a continuous curve. When all of the interspecies interactions conform to the Lorentz-Berthelot rules, the mixture phase separates into one solid phase and one liquid phase over a range of compositions. In this case, the curves on the ternary phase diagram indicating the composition of the solid and liquid phases extend continuously from the diastereomer 1–solvent edge of the diagram to the diastereomer 2–solvent edge of the diagram. When the interspecies diameter is increased to that of the larger diastereomer, the resulting phase diagram is similar, except that there is an increase in the solubility of the diastereomers in the solvent. When the interspecies well-depth is lowered to less than that of either of the diastereomers, two solid phases are formed along the diastereomer 1—diastereomer 2 edge of the diagram. This immiscibility between the solid-phases extends into the ternary phase diagram and results in the formation of a three-phase region. When ternary phase diagrams are calculated at a series of temperatures, it is found that as the temperature increases, the size of this three-phase region decreases until it disappears. It is also found that at low temperatures a solvent-rich solid is formed which disappears as the temperature increases. At high temperatures the pure solvent forms a gas and the ternary phase diagram contains a region of equilibrium between solvent-rich vapor and diastereomer-rich liquid. For a limited range of solvent concentration and temperature, one of the diastereomers precipitates from an equimolar mixture of the diastereomers in the solvent. This implies that for that range of temperature and composition, one of the diastereomers can be separated from the mixture. The purity of the precipitate is found to increase as the temperature decreases.

Method

The Gibbs-Duhem integration technique is based upon numerically integrating an appropriate form of the Clapeyron equation, which determines how the field variables vary as a function of each other at equilibrium. One can calculate the properties of two coexisting phases as a function of almost any variable of interest. For a mixture of components, the Gibbs-Duhem equation[10] can be expressed as

$$d\ln\left[\sum_{i=1}^{c}\hat{f}_i\right] = h_{\mathrm{r}}\mathrm{d}\beta + Z d\ln p - \sum_{i=1}^{c}\frac{x_i}{\xi_i}d\xi_i \tag{1}$$

where p is the pressure, Z is the compressibility factor, x_i, f_i the mole fraction and fugacity of species i, h_{r} is the residual molar enthalpy, $\beta = 1/kT$ where β is the temperature, and ξ_i is the fugacity fraction, defined as

$$\xi_i = \frac{\hat{f}_i}{\sum_{n=1}^{c}\hat{f}_n}. \tag{2}$$

For ternary mixtures Eq. 1 reduces to the following

$$d\ln(f_1+f_2+f_3) = h_r d\beta + Z d\ln p - \frac{x_1}{\xi_1}d\xi_1 - \frac{x_2}{\xi_2}d\xi_2 - \frac{x_3}{\xi_3}d\xi_3 \tag{3}$$

The Gibbs-Duhem equations can be applied to two phases, α and γ, in equilibrium, by writing Eq. 3 for each of the phases. Since the fugacity, and hence the fugacity fraction, of each of the components is identical in phases α and γ, we can set the right hand sides of those two equations equal to get

$$h_{\mathrm{r}}^{\alpha}d\beta + Z^{\alpha}d\ln p - \frac{x_1^{\alpha}}{\xi_1}d\xi_1 - \frac{x_2^{\alpha}}{\xi_2}d\xi_2 - \frac{x_3^{\alpha}}{\xi_3}d\xi_3 = h_{\mathrm{r}}^{\gamma}d\beta + Z^{\gamma}d\ln p - \frac{x_1^{\gamma}}{\xi_1}d\xi_1 - \frac{x_2^{\gamma}}{\xi_2}d\xi_2 - \frac{x_3^{\gamma}}{\xi_3}d\xi_3 \tag{4}$$

At this point there are several integration pathways to choose, depending upon which properties are held fixed and

which are allowed to vary. Because we are interested in calculating ternary phase diagrams at constant temperature and pressure, we choose to hold temperature and pressure fixed, which results in

$$\frac{x_1^\alpha}{\xi_1}d\xi_1+\frac{x_2^\alpha}{\xi_2}d\xi_2+\frac{x_3^\alpha}{\xi_3}d\xi_3=\frac{x_1^\gamma}{\xi_1}d\xi_1+\frac{x_2^\gamma}{\xi_2}d\xi_2+\frac{x_3^\gamma}{\xi_3}d\xi_3 \quad (5)$$

Using the relations $x_3 = 1 - x_1 - x_2$ and $\xi_3 = 1 - \xi_1 - \xi_2$ we can eliminate x_3 and ξ_3 from Eq. 5 and write

$$\frac{d\xi_1}{d\xi_2}=\frac{\Delta x_2(1-\xi_1)\xi_1+\Delta x_1\xi_1\xi_2}{\Delta x_1(1-\xi_2)\xi_2+\Delta x_2\xi_1\xi_2} \quad (6)$$

where $\Delta x_i = x_i^\alpha - x_i^\alpha$.

The integration is typically started at $\xi_2 = 0$. The initial condition is then two phases, α and γ, each a mixture of components 1 and 3, in equilibrium at the chosen temperature and pressure, as indicated by the large dots in Figure 1. The initial condition fugacity fractions and compositions used in Eq. 6 can be determined by carrying out a binary Gibbs Duhem integration for a mixture of components 1 and 3, as explained in a previous paper.[13] The right hand side of Eq. 6 is undefined as $\xi_2 \to 0$. To remedy this, we divide the top and bottom of the right hand side of Eq. 6 by ξ_2 to get

$$\frac{d\xi_1}{d\xi_2}=\frac{\frac{\Delta x_2}{\xi_2}(1-\xi_1)\xi_1+\Delta x_1\xi_1}{\Delta x_1(1-\xi_2)+\Delta x_2\xi_1} \quad (7)$$

which can be written in terms of Henry's constants since as $\xi_2 \to 0$ (and hence $x_2 \to 0$ for the α and γ phases) $f_2 \to x_2H_2$ where H_2 is the Henry's constant of component 2 in the mixture. It follows then that

$$\left.\frac{d\xi_1}{d\xi_2}\right|_{\xi_2=0}=-\frac{\left[\left(\frac{x_2}{x_2H_2/(f_1+f_3)}\right)^\alpha-\left(\frac{x_2}{x_2H_2/(f_1+f_3)}\right)^\gamma\right](1-\xi_1)\xi_1+\Delta x_1\xi_1}{\Delta x_1(1-\xi_2)+\Delta x_2\xi_1} \quad (8)$$

Here we have made use of the fact that $\xi_2^\alpha = \xi_2^\gamma$. Recognizing that $\Delta x_2 = 0$ when $\xi_2 = 0$, this can be further reduced to

$$\left.\frac{d\xi_1}{d\xi_2}\right|_{\xi_2=0}=-\frac{\left[\left(\frac{f_1}{H_2}+\frac{f_3}{H_2}\right)^\alpha-\left(\frac{f_1}{H_2}+\frac{f_3}{H_2}\right)^\gamma\right](1-\xi_1)\xi_1+\Delta x_1\xi_1}{\Delta x_1} \quad (9)$$

where f_1/H_2 and f_3/H_2 can be calculated by conducting an NPT simulation on each of the mixtures. We can calculate $(f_1/H_2)^\alpha$ and $(f_3/H_2)^\alpha$ by calculating the change in potential energy upon switching a particle of component 1 to component 2 and a particle of component 3 to component 2, respectively, at the temperature, pressure, and composition of phase α. The values of $(f_1/H_2)^\alpha$ and $(f_3/H_2)^\alpha$ can be calculated from

$$\frac{f_i}{H_2}=\langle \exp\left(\Delta U_{i\to 2}/kT\right)\rangle_{\mathrm{NPT}} \quad (10)$$

where $\langle\rangle$ denotes the ensemble average and $U_{i\to 2}$ is the potential energy change upon switching the identity of a particle from component i (i = 1 or 3) to component 2. The same procedure can then be used to calculate the values of $(f_1/H_2)^\gamma$ and $(f_3/H_2)^\gamma$.

Once the initial condition is calculated, the integration is carried out using a standard predictor–corrector algorithm. A step, $\Delta\xi_2$, in the fugacity fraction of component 2 is taken and the trapezoid-rule predictor formula is used to find the new value for the fugacity fraction of component 1, ξ_1^1, i.e.

$$\xi_1^1=\xi_1^0+\left(\xi_2^1-\xi_2^0\right)\left(\frac{d\xi_1}{d\xi_2}\right)^0 \quad (11)$$

where ξ_1^0 is the value of the fugacity fraction of component 1 at the initial condition and $d\xi_1/d\xi_2$ is calculated from Eq. 9. The step size, $\Delta\xi_2$, used is typically chosen such that $\Delta\xi_2 \cdot d\xi_1/d\xi_2 \approx 0.2$. A separate semigrand ensemble (constant NPTξ_2) Monte Carlo simulation is then performed for each of the coexisting phases at the new values of ξ_1 and ξ_2. The simulations, explained in more detail later, are carried out in such a manner that the equilibrium values of the composition of each mixture result directly from the simulations as a consequence of the identity exchange moves. After the simulations have equilibrated, the new values of Δx_1 and Δx_2 as well as ξ_1 and ξ_2 are used to compute the value of the integrand (Eq. 6). The trapezoid-rule corrector formula

$$\xi_1^1=\xi_1^0+\frac{\xi_2^1-\xi_2^0}{2}\left[\left(\frac{d\xi_1}{d\xi_2}\right)^1+\left(\frac{d\xi_1}{d\xi_2}\right)^0\right] \quad (12)$$

is then applied to find the "corrected" value of ξ_1. Another pair of simulations are then performed at this new value of ξ_1 (the value of ξ_2 has not changed at this point) to deter-

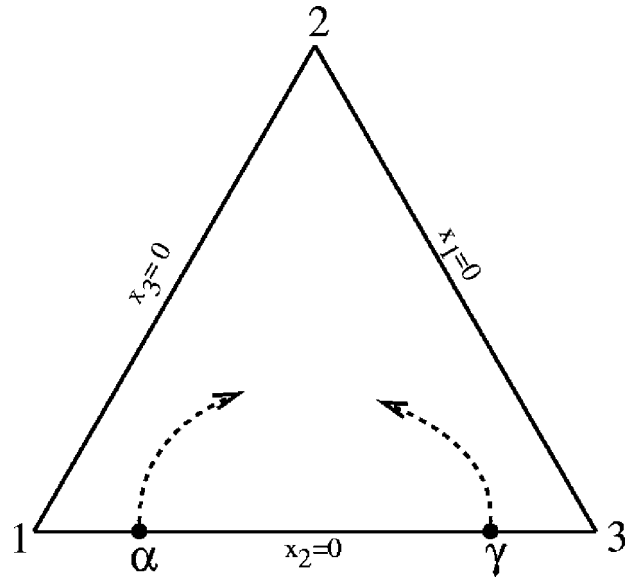

Figure 1. Schematic of ternary Gibbs Duhem integration.

The dots indicate the compositions of the initial coexisting phases. The dashed lines indicate the coexistence curves.

mine the equilibrium compositions of the mixtures. This corrector step is repeated until ξ_1 converges to its final value. A production run of simulations is then carried out to calculate the final values of the compositions of the coexisting phases. Another step, $\Delta\xi_2$, in the fugacity fraction of component 2 is taken and the predictor–corrector algorithm is used to calculate the new value of ξ_1. As more state points are known the integration proceeds using higher order predictor–corrector algorithms, such as the Adams-Bashford predictor and Adams-Moulton corrector formulas,[14] respectively

$$\xi_1^{n+1} = \xi_1^n + \frac{\xi_2^{n+1} - \xi_2^n}{24}\left[55\left(\frac{d\xi_1}{d\xi_2}\right)^n - 59\left(\frac{d\xi_1}{d\xi_2}\right)^{n-1} + 37\left(\frac{d\xi_1}{d\xi_2}\right)^{n-2} - 9\left(\frac{d\xi_1}{d\xi_2}\right)^{n-3}\right] \quad (13)$$

and

$$\xi_1^{n+1} = \xi_1^n + \frac{\xi_2^{n+1} - \xi_2^n}{24}\left[9\left(\frac{d\xi_1}{d\xi_2}\right)^{n+1} + 19\left(\frac{d\xi_1}{d\xi_2}\right)^n - 5\left(\frac{d\xi_1}{d\xi_2}\right)^{n-1} + \left(\frac{d\xi_1}{d\xi_2}\right)^{n-2}\right] \quad (14)$$

where the superscripts denote the calculated coexistence states, with $(n+1)$ being the current state point. Continuing this process we can calculate the entire phase coexistence envelope. We tested our method by comparing results calculated using the Gibbs Duhem integration technique to those calculated by Tsang et al.,[15] using the Gibbs ensemble technique. There was excellent agreement between the two methods.

Semigrand ensemble Monte Carlo simulations are used to evaluate the properties of the coexisting phases during the integration of the Gibbs-Duhem equation. There are three types of moves in the semigrand ensemble: particle displacement, volume change, and identity exchange. The particle displacement and volume change moves are carried out in the same manner as in isothermal-isobaric (NPT) simulations. The identity exchange move involves choosing a random molecule in the system and changing its identity to that of one of the other species in the mixture chosen at random (for the binary case, this is simply the other species). The change in the configurational energy of the system caused by the identity change is then evaluated. For mixtures of molecules of similar size and shape, such as presented in this article, the identity swap can be done in a single step without much difficulty. However for mixtures of molecules of rather dissimilar size and shape, the probability of acceptance of an identity swap can become prohibitively low, especially in the solid-phase. Kofke proposes a second, osmotic, form of ensemble that may be used to overcome this problem.[11] The overall acceptance probability, P, for any of these moves is

$$\mathcal{P} = \min\left[1, \exp\left(-\beta\left(U^{\text{trial}} - U^{\text{old}}\right) - \beta P\left(V^{\text{trial}} - V^{\text{old}}\right) + N\ln\frac{V^{\text{trial}}}{V^{\text{old}}} + \ln\frac{\xi_{\text{trial}}}{\xi_{\text{old}}}\right)\right] \quad (15)$$

where U^{trial} and U^{old} are the configurational energies, V^{trial} and V^{old} are the volumes of the trial and existing states respectively, N is the total number of molecules, and ξ_{trial} and ξ_{old} refer to the fugacity fractions of the trial and existing identities of the molecule during the identity exchange moves. At each step, the type of move is randomly chosen with a weighting such that for every volume change move there are 20 particle displacements and 20 identity exchange moves. After an appropriate number of equilibrium moves, a running average of the composition is calculated for use in computing the integrand in the Gibbs Duhem technique.

Other details of the simulations are as follows. Each simulation box contains 2048 molecules. A cell structured neighbor list[16] is used to increase the efficiency of the simulations. Prior theoretical calculations[17] and molecular simulations,[18] have shown that by choosing diameter ratios $0.85 \leq \sigma_{11}/\sigma_{22} \leq 1.0$ we can assume that the most stable configuration for the solid-phase is a substitutionally disordered fcc lattice. By using an fcc lattice as an initial configuration for the solid-phase, the fcc lattice is maintained in the solid-phase throughout the simulation without any additional constraints on the simulation. The simulations are conducted in a cubic box with periodic boundary conditions. The molecules interact via the Lennard-Jones potential

$$u_{ij}(r) = 4\varepsilon_{ij}\left[\left(\frac{\sigma_{ij}}{r}\right)^{12} - \left(\frac{\sigma_{ij}}{r}\right)^{6}\right] \quad (16)$$

where u_{ij} is the potential energy of the interaction between atoms i and j, r is the distance between atoms i and j, ε_{ij} is the Lennard-Jones well-depth, and σ_{ij} is the Lennard-Jones diameter. The potential interactions are truncated at half the box length and standard long range corrections[15] are applied to the potential and pressure calculations.

Results

We have calculated phase diagrams for three different ternary mixtures containing two model diastereomers (species 1 and 2) and a solvent (species S). The pure component properties and solvent-diastereomer interaction parameters (see Table 1) are the same in the three mixtures. The two diastereomer molecules have similar size and melting point, much like the diastereomers in a real mixture would. The solvent well-depth and size were chosen so that the solvent would have a lower melting point than the diastereomers and be somewhat smaller. The cross-species parameters between the diastereomers were varied, as explained later. All three of

Table 1. Lennard-Jones Parameters Used in Figures 1 and 2

	Set 1	Set 2	Set 3
ε_{11}	2.000	2.000	2.000
ε_{22}	2.050	2.050	2.050
ε_{SS}	1.000	1.000	1.000
ε_{1S}	1.414	1.414	1.414
ε_{2S}	1.432	1.432	1.432
ε_{12}	2.025	2.025	1.822
σ_{11}	1.150	1.150	1.150
σ_{22}	1.175	1.175	1.175
σ_{SS}	1.000	1.000	1.000
σ_{1S}	1.075	1.075	1.075
σ_{2S}	1.088	1.088	1.088
σ_{12}	1.163	1.175	1.163

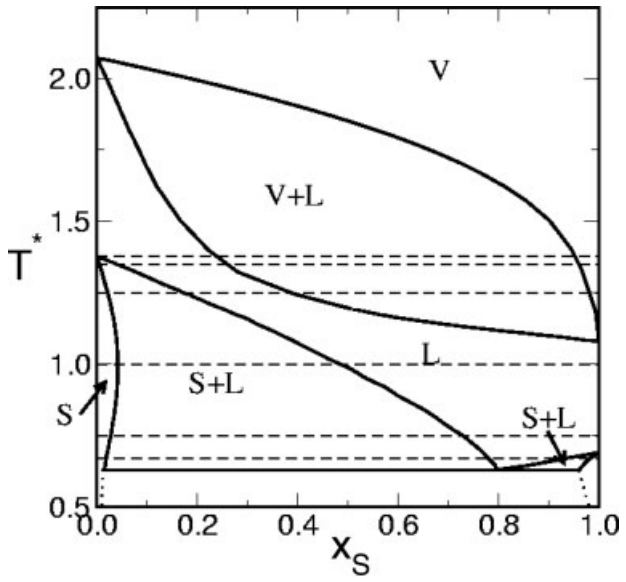

Figure 2. Binary phase diagram of component 1 and the solvent at $P^* = 0.040$.

The dashed lines indicate the temperatures at which the following ternary phase diagrams are calculated.

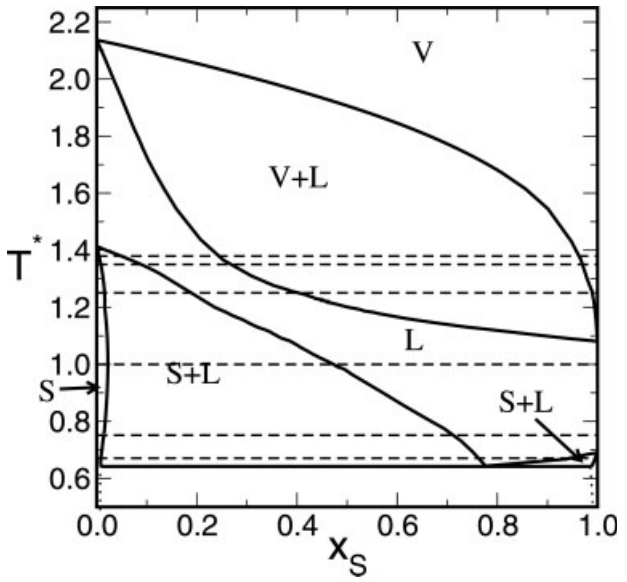

Figure 3. Binary phase diagram of component 2 and the solvent at $P^* = 0.040$.

The dashed lines indicate the temperatures at which the following ternary phase diagrams are calculated.

the diagrams were calculated at a constant pressure, $P^* \equiv P\sigma_{SS}^3/\varepsilon_{ss} = 0.04$, and temperature, $T^* \equiv kT/\varepsilon_{ss} = 1.000$. To determine the initial conditions for use in the Gibbs Duhem calculation of the ternary phase diagrams, three binary mixtures were considered components as follows: component 1+ solvent (Figure 2); component 2+ solvent (Figure 3); and component 1+ component 2 (Figure 4); temperature–composition phase diagrams were calculated. This gave us the properties of the coexisting phases along the edges of the ternary phase diagrams.

Figure 5 is the ternary phase diagram calculated when $\varepsilon_{12} = 2.025$ and $\sigma_{12} = 1.163$, which corresponds to the Lorentz-Berthelot mixing rules, $\varepsilon_{12} = (\varepsilon_{11}\varepsilon_{22})^{1/2}$ and $\sigma_{12} = (\sigma_{11} + \sigma_{22})/2$. This is set 1 on Table 1. The diagram shows a liquid-phase in the solvent rich region, a single solid-phase in the solvent poor region, and a two-phase solid–liquid region in between. In the diagram, the upper and lower lines indicate the compositions of the liquid and solid in equilibrium. Tie lines connect approximately every fifth set of coexisting points to make the diagram easier to read. Mixtures in the two-phase region phase separate into a liquid and solid phase with compositions determined by the tie line that crosses the total composition of the system. Mixtures whose composition is in the region below the solid line exist as a substitutionally disordered fcc lattice crystal. One can see that the solid rich in component 1 (lower right corner) contains slightly more solvent than the solid rich in component 2 (lower left corner). This can be explained by the greater difference in size and well-depth between component 2 and the solvent than between component 1 and the solvent. As the difference between the well-depths (and hence critical points) of two components in a binary mixture becomes greater, the two components become less miscible with each other.

Figure 6 is the ternary phase diagram calculated when $\varepsilon_{12} = 2.025$ and $\sigma_{12} = 1.175$, which means the interspecies diameter is equal to the diameter of the second component. This is set 2 on Table 1. Physically, this means that there will be greater repulsion at close range between a species of component 1 and a species of component 2 than there was in the previous case (Figure 5). This diagram looks fairly similar to Figure 5 except that the solid is slightly less soluble in the mixture than in Figure 5, i.e. the liquid in coexistence with the solid is richer in both components, as indicated by the minimum in the liquid curve. Since σ_{12} in Figure 6 is

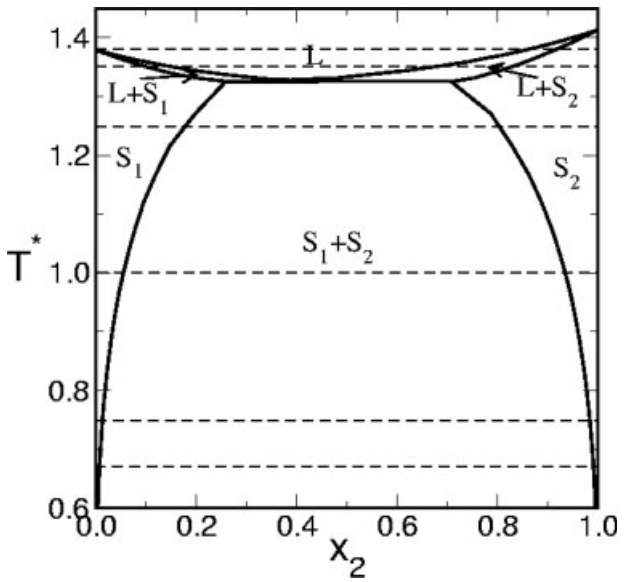

Figure 4. Binary phase diagram of component 1 and component 2 at $P^* = 0.040$.

The dashed lines indicate the temperatures at which the following ternary phase diagrams are calculated.

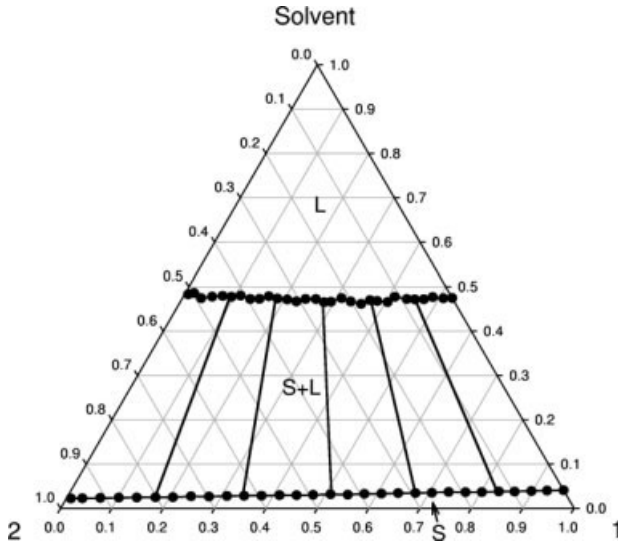

Figure 5. Ternary phase diagram calculated at T^* = 1.00, P^* = 0.040 and ε_{12} = 2.025, σ_{12} = 1.163.

larger than in Figure 5 the molecules no longer pack as tightly in the solid, which leads to a decreased effective attraction between components 1 and 2. Consequently, the enthalpic penalty for entering the liquid phase is no longer as great and the solid becomes more soluble.

Figures 7–12 are ternary phase diagrams calculated at a series of temperatures, kT/ε_{SS} = 0.67, 0.75, 1.00, 1.25, 1.35, and 1.38, for a mixture with ε_{12} = 1.822 and σ_{12} = 1.163. This is set 3 on Table 1. The lower graph in each figure is a schematic of the actual data presented in the upper graph. In this case, the intraspecies diastereomeric attraction, ε_{12}, is stronger than the interspecies diastereomeric attraction, or in terms of deviation from Lorentz-Berthelot mixing rules, k_{12} = 0.9, where $\varepsilon_{12} = (1 - k_{12})(\varepsilon_{11}\varepsilon_{22})^{1/2}$. The horizontal lines on Figures 2–4 indicate the series of temperatures at which the ternary phase diagrams are calculated.

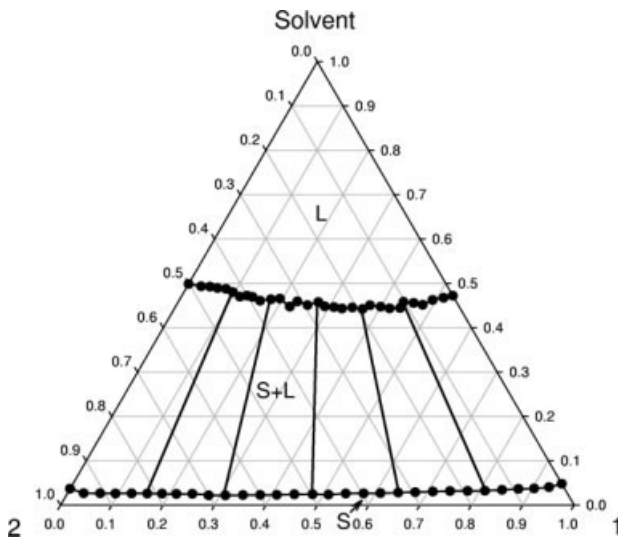

Figure 6. Ternary phase diagram calculated at T^* = 1.00, P^* = 0.040 and ε_{12} = 2.025, σ_{12} = 1.175.

Figure 7 is the ternary phase diagram calculated at a reduced temperature of kT/ε_{SS} = 0.67. At this temperature in the binary component 1–component 2 phase diagram (Figure 4), the solids formed at low temperature phase separate into two solid solutions. In both the component 1–solvent and component 2–solvent (Figures 2 and 3) binary phase diagrams there are two regions of solid–liquid phase equilibria, one with a solvent-rich solid and one with a solid rich in component 1 (or 2). It can be seen in Figure 7 that the solid–solid immiscibility in the absence of solvent (bottom of diagram) is decreased upon the addition of the solvent and that the solid–solid immiscibility curves intersect with the solid–liquid coexistence curves originating from the component 1–solvent and component 2–solvent edges of the ternary phase diagram, resulting in a three-phase region. Mixtures within the three-phase region will phase separate into two solid phases and one liquid phase whose compositions are given by the vertices of the triangle forming the three-phase region. There also exists a region of solid–liquid phase equilibrium near the pure solvent vertex of the ternary phase diagram.

Figure 8 is the ternary phase diagram calculated at a reduced temperature of kT/ε_{SS} = 0.75. At this temperature in the binary component 1–component 2 phase diagram (Figure 4), the solids

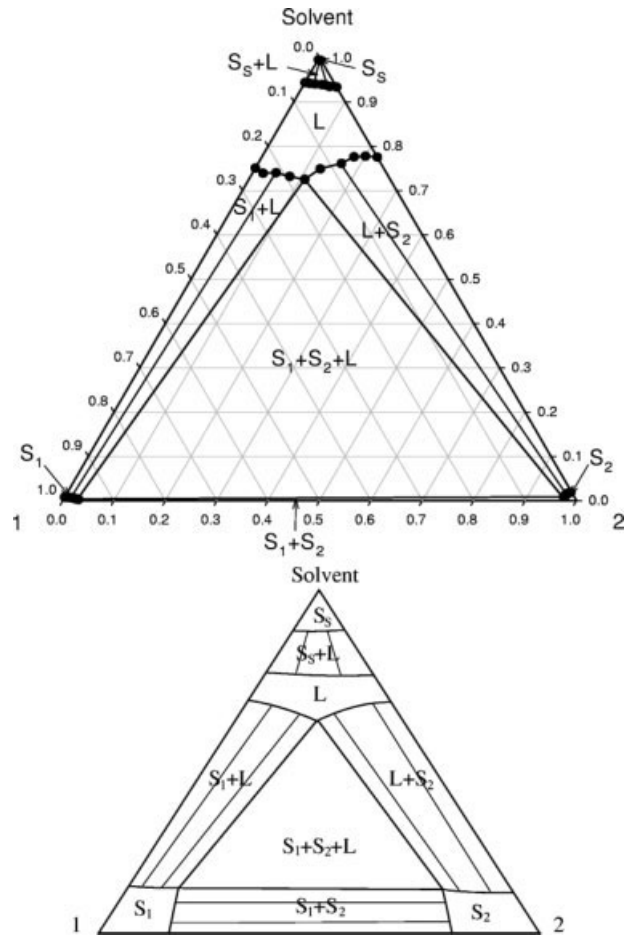

Figure 7. Ternary phase diagram calculated at T^* = 0.67, P^* = 0.040 and ε_{12} = 1.822, σ_{12} = 1.163.

The upper graph is data calculated by the Gibbs Duhem integration technique and the bottom graph is a schematic of the upper graph.

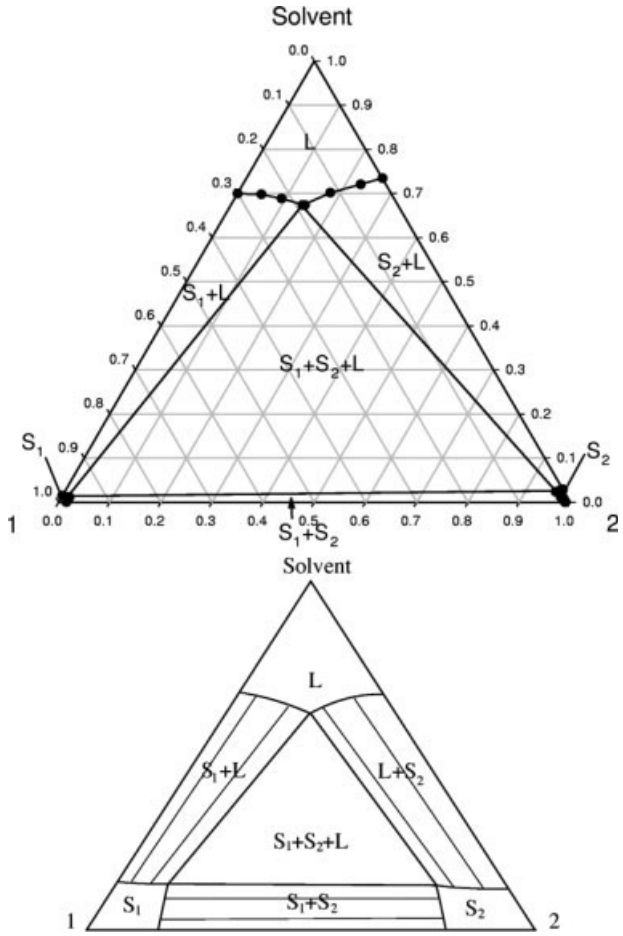

Figure 8. Ternary phase diagram calculated at T^* = 0.75, P^* = 0.040 and ε_{12} = 1.822, σ_{12} = 1.163.

The upper graph is data calculated by the Gibbs Duhem integration technique and the bottom graph is a schematic of the upper graph.

formed at low temperature phase separate into two solid solutions, although the solids are not as pure as at kT/ε_{SS} = 0.67 (Figure 7). In both the component 1–solvent and component 2–solvent binary phase diagrams (Figures 2 and 3) there is only one region of solid–liquid phase equilibria. As a result there is no longer a solid rich in solvent in the ternary phase diagram. The diastereomers have become more soluble in the solvent as indicated by the higher mole fraction of diastereomers in the liquid coexisting with the solid, and the region of three phase coexistence is smaller than at the previous temperature.

Figure 9 is the ternary phase diagram calculated at a reduced temperature of kT/ε_{SS} = 1.00. At this temperature in the binary component 1–component 2 phase diagram (Figure 4), the solids formed at low temperature phase separate into two solid solutions. In both the component 1–solvent and component 2–solvent binary phase diagrams (Figures 2 and 3) there is one region of solid–liquid phase equilibria. Figure 9 is similar to Figure 8 except that the diastereomers are again more soluble and the solids are less pure, resulting in a three-phase region smaller than at the previous temperature.

Figure 10 is the ternary phase diagram calculated at a reduced temperature of kT/ε_{SS} = 1.25. At this temperature in the binary component 1–component 2 phase diagram (Figure 4), the solids formed at low temperature phase separate into two solid solutions of even lower purity that at kT/ε_{SS} = 1.00 (Figure 9). In both the component 1–solvent and component 2–solvent binary phase diagrams (Figures 2 and 3) there is one region of solid–liquid phase equilibria and one region of vapor–liquid phase equilibria. Because of the vapor–liquid equilibria present in the binary phase diagrams, a region of vapor–liquid phase equilibria forms in the ternary phase diagram at high concentrations of solvent. The region of three-phase phase equilibria is even smaller than it was at the previous temperature.

Figure 11 is the ternary phase diagram calculated at a reduced temperature of kT/ε_{SS} = 1.35. At this temperature in the binary component 1–component 2 phase diagram (Figure 4), there are two regions of solid–liquid phase equilibria, which means that there are two pairs of curves emanating from the component 1–component 2 edge of the ternary phase diagram. In both the component 1–solvent and component 2–solvent binary phase diagrams (Figures 2 and 3) there is one region of solid–liquid phase equilibria and one region of vapor–liquid phase equilibria. Because there is no longer

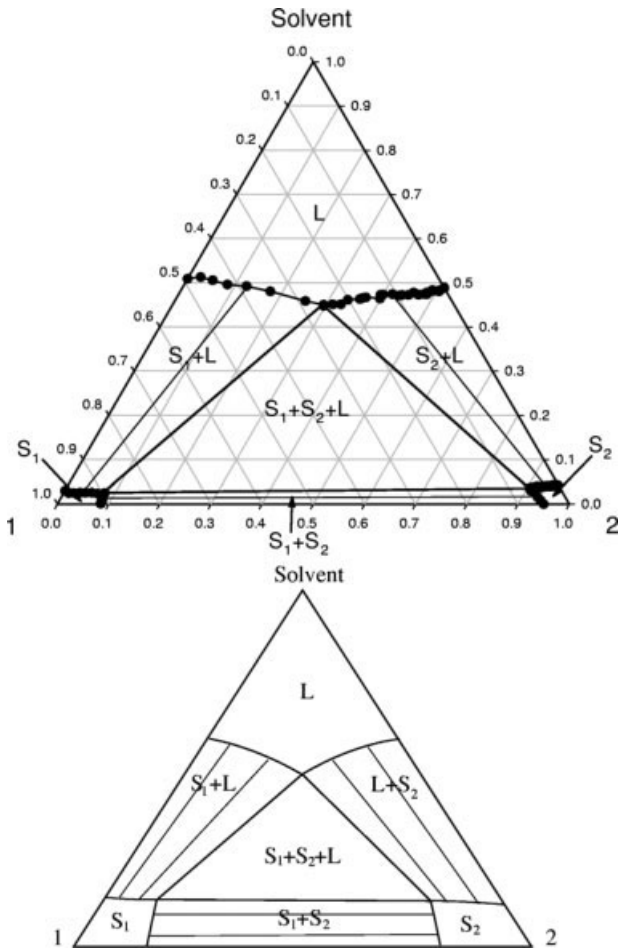

Figure 9. Ternary phase diagram calculated at T^* = 1.00, P^* = 0.040 and ε_{12} = 1.822, σ_{12} = 1.163.

The upper graph is data calculated by the Gibbs Duhem integration technique and the bottom graph is a schematic of the upper graph.

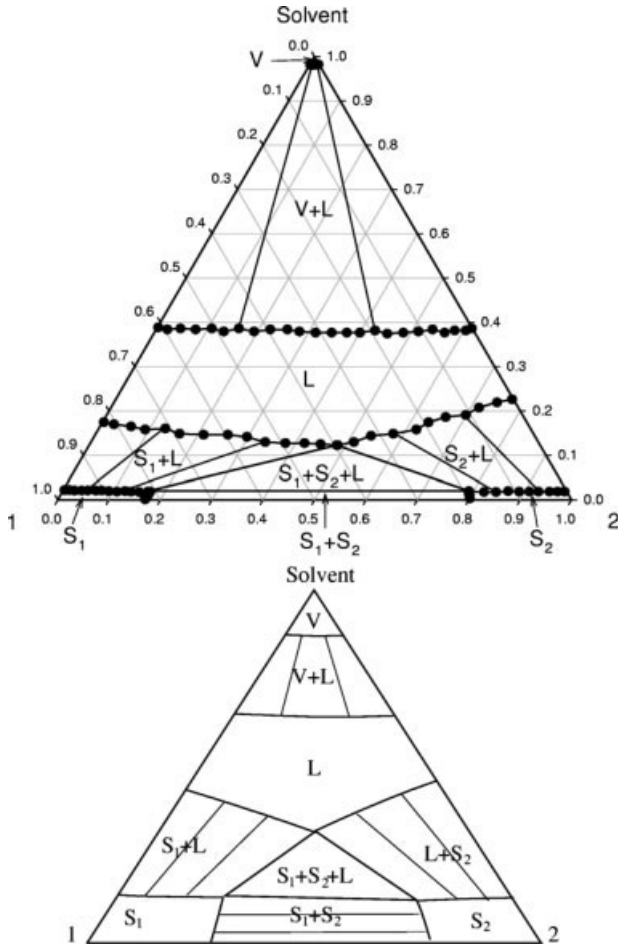

Figure 10. Ternary phase diagram calculated at T^* = 1.25, P^* = 0.040 and ε_{12} = 1.822, σ_{12} = 1.163.

The upper graph is data calculated by the Gibbs Duhem integration technique and the bottom graph is a schematic of the upper graph.

any solid–solid phase coexistence in the binary component 1–component 2 phase diagram, the three-phase region has disappeared. At high concentrations of solvent there is a region of vapor–liquid phase coexistence; the liquid phase solvent concentration here is lower than in the previous case. At low concentrations of solvent there are two separate regions of solid–liquid phase equilibria.

Figure 12 is the ternary phase diagram calculated at a reduced temperature of kT/ε_{SS} = 1.38. At this temperature in the binary component 1–component 2 phase diagram (Figure 4), there is one region of solid–liquid phase equilibria. In the component 1–solvent binary phase diagram (Figure 2) there is only one region of vapor–liquid equilibria, while in the component 2–solvent binary phase diagram (Figure 3) there is one region of solid–liquid equilibria and one region of vapor–liquid equilibria. At high concentrations of solvent in the ternary phase diagram there is a region of vapor–liquid phase coexistence and the concentration of solvent in the liquid phase is again slightly lower than at the previous temperature. At low concentrations of solvent there is now only one region of solid–liquid phase equilibria.

To apply the previous figures to the process of classical resolution, one must consider that a racemic mixture will, in most cases, be an equimolar mixture of the two racemates. Consequently, the mixture that results from reacting with the enantiomers with the resolving agent will be an equimolar mixture of the two diastereomers. In terms of the ternary diagrams that have been presented, the composition of the mixtures will fall upon a line that extends from the pure solvent vertex of the ternary phase diagram to the middle of the component 1–component 2 edge of the diagram. In Figures 7–10, we see that there exists a range of solvent concentration along this line where the mixture phase separates into a liquid and a solid rich in one of the two components, shifting from component 1 to component 2 as the temperature increases. It is for this range of solvent concentration that separation of the diastereomers is possible. For example, in Figure 7 mixtures with an equal concentration of the diastereomers and a solvent mole fraction between 0.69 and 0.75 will separate into a solid phase rich in component 2 and a liquid phase.

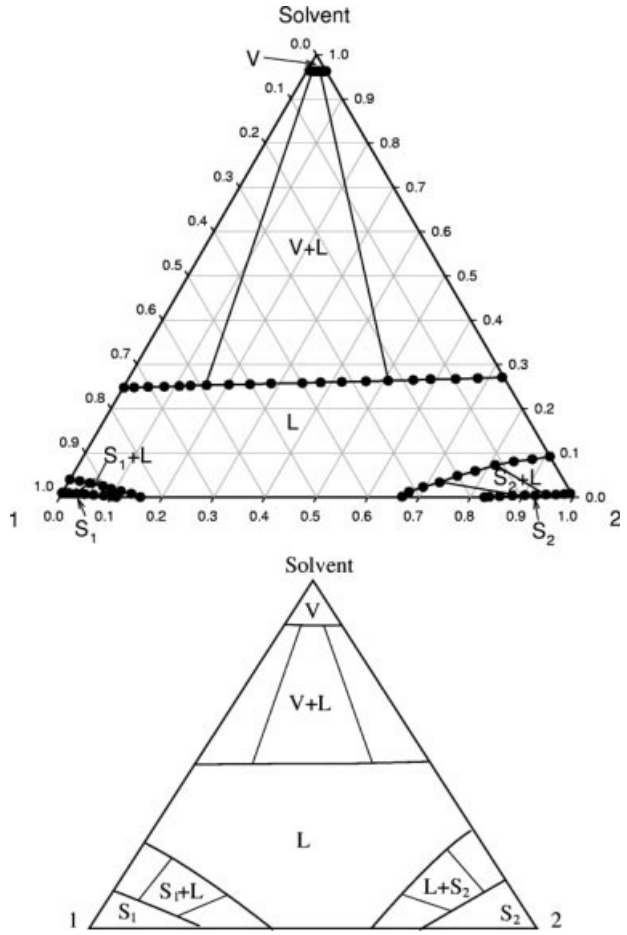

Figure 11. Ternary phase diagram calculated at T^* = 1.35, P^* = 0.040 and ε_{12} = 1.822, σ_{12} = 1.163.

The upper graph is data calculated by the Gibbs Duhem integration technique and the bottom graph is a schematic of the upper graph.

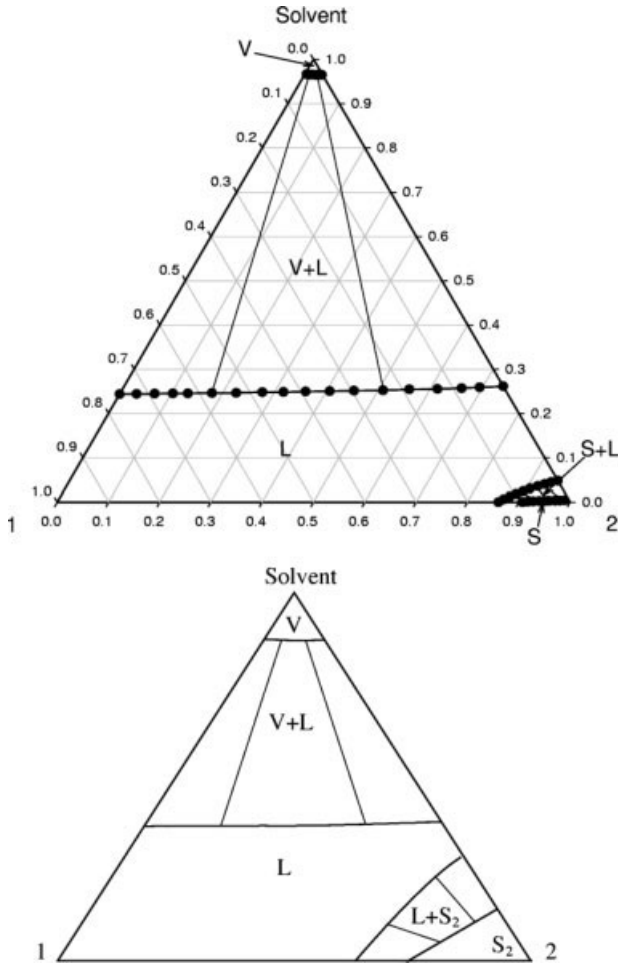

Figure 12. Ternary phase diagram calculated at $T^* = 1.38$, $P^* = 0.040$ and $\varepsilon_{12} = 1.822$, $\sigma_{12} = 1.163$.

The upper graph is data calculated by the Gibbs Duhem integration technique and the bottom graph is a schematic of the upper graph.

Summary

We extended the Gibbs Duhem integration technique to calculate ternary phase equilibria at constant temperature and pressure. We applied the technique to the calculation of ternary phase equilibria for a model diastereomeric system composed of two "diastereomers" of similar size and melting point and a "solvent" of slightly smaller size and lower melting temperature. The cross-species well-depth and diameter between the two diastereomers were varied to determine their impact on the resulting phase equilibria. We found that increasing the interspecies diameter up to that of the larger component resulted in a slight increase in the solubility of the solvent. When the interspecies well-depth was lowered to below that of either of the diastereomers, two immiscible solid phases were formed resulting in a region of three-phase equilibria in the ternary phase diagram. We then calculated a series of ternary phase diagrams at various temperatures for the same set of intermolecular parameters. It was found that as the temperature increases, the size of the three-phase region decreases until it disappears. It was also found that at low temperatures a solvent-rich solid is formed which disappears as the temperature increases. At high temperatures a solvent-rich gas was formed and this resulted in a region of equilibrium between solvent-rich vapor and diastereomer-rich liquid. For a limited range of concentration of solvent and temperature, one of the diastereomers will precipitate from an equimolar mixture of the diastereomers in the solvent.

Acknowledgments

We are grateful to Drs. Maurico Futran, Ronald Zumstein, and Peter Kilpatrick for stimulating discussions. This work was supported by the Office of Energy Research, Basic Energy Sciences, Chemical Sciences Division of the U.S. Department of Energy under Contract No. DE-FG02-97ER14771. Acknowledgment is also made to the Donors of the Petroleum Research Fund administered by the American Chemical Society for partial support of this work.

Literature Cited

1. Collet A. Separation and purification of enantiomers by crystallization methods. *Enantiomer*. 1999;4:157–172.
2. Stinson SC. Chiral drugs. *Chem Eng News*. 1995;73:44–74.
3. Lorenz H, Seidel-Morgenstern A. Binary and ternary phase diagrams of two enantiomers in solvent systems. *Thermochim Acta*. 2002;382:129–142.
4. Schroer JW, Wibowo C, Ng KM. Synthesis of chiral crystallization processes. *AIChE J*. 2001;47:369–387.
5. Leitao MLP, Eusebio ME, Maria TMR, Redinha JS. Solid + liquid phase diagram for trans-1,2-cyclohexanediol enantiomer mixtures. *J Chem Thermodyn*. 2002;34:557–568.
6. Cottin X, Paras PA, Vega C, Monson PA. Solid-fluid equilibrium: new perspectives from molecular theory. *Fluid Phase Equil*. 1996;117:114–125.
7. Ericsson B, Hallmans B. Treatment of saline wastewater for zero discharge at the debiensko coal mines in Poland. *Desalination*. 1996;105:115–123.
8. Takano K, Gani R, Ishikawa T, Kolar P. Conceptual design and analysis methodology for crystallization processes with electrolyte systems. *Fluid Phase Equil*. 2002;194–197:783–803.
9. Kofke DA. Direct evaluation of phase coexistence by molecular simulation via integration along the saturation line. *J Chem Phys*. 1993;98:4149–4162.
10. Kofke DA. Gibbs-Duhem integration: a new method for direct evaluation of phase coexistence by molecular simulation. *Mol Phys*. 1993;78:1331–1336.
11. Mehta M, Kofke DA. Coexistence diagrams of mixtures by molecular simulation. *Chem Eng Sci*. 1994;49:2633–2645.
12. Hitchcock MR, Hall CK. Solid–liquid phase equilibrium for binary Lennard-Jones mixtures. *J Chem Phys*. 1999;110:11433–11444.
13. Attwood BC, Hall CK. Effect of the solid phase on the global phase behavior of binary Lennard-Jones mixtures. *AIChE J*. 2004;50:1948–1960.
14. Rice RG, Do DD. *Applied Mathematics and Modeling for Chemical Engineers*. New York, NY: Wiley, 1995.
15. Tsang PC, White ON, Perigard BY, Vega LF, Panagiotopolous AZ. Phase equilibria in ternary Lennard-Jones systems. *Fluid Phase Equil*. 1995;107:31–43.
16. Allen MP, Tildesley DJ. *Computer Simulation of Liquids*. New York: Oxford Science Publications, 1997.
17. Cottin X. A theoretical study of the thermodynamics of solid solutions and solid-liquid phase equilibria, PhD thesis, University of Massachusetts, 1996.
18. Kranendonk WGT, Frenkel D. Computer simulation of solid-liquid coexistence in binary hard-sphere mixtures. *Mol Phys*. 1991;72:679–697.

Manuscript received Mar. 19, 2008.